Journal of Materials Chemistry A

PAPER

View Article Online
View Journal | View Issue

Cite this: J. Mater. Chem. A, 2016, 4, 15968

Hierarchical porous microspheres of activated carbon with a high surface area from spores for electrochemical double-layer capacitors

Yiyi Jin,† Kuan Tian,† Lu Wei,* Xingyan Zhang and Xin Guo*

Received 12th July 2016
Accepted 9th September 2016

DOI: 10.1039/c6ta05872h

www.rsc.org/MaterialsA

Owing to the advantages of high surface area, good conductivity, sustainability, and chemical stability, biomass-based activated carbon materials have been one of the research hotspots in the field of supercapacitors. Yet common techniques to synthesize nanostructured electrodes of activated carbon only offer limited control on their morphology and structure. In this work, three-dimensional porous hollow microspheres of activated carbon are fabricated by utilizing various spores (*Lycopodium clavatum*, *Ganodorma lucidum* and *Lycopodium annotinum* spores) as carbon precursors and self-templates through a facile, green and low-cost route. The abundant and easily available carbon sources of spores allow for mass production of activated carbon microspheres (ACMs), which almost ideally inherit the distinctive nano-architectures of spores, presenting a superhigh specific surface area (up to 3053 m^2 g^{-1}) and hierarchical porous structure. Such ACM electrodes show remarkable electrical double-layer storage performances, such as high specific capacitance (308 F g^{-1} in organic electrolytes), ultrafast rate capability (retaining 263 F g^{-1} at a very high current density of 20 A g^{-1}) and good cycling stability (93.8% retention after 10 000 charge–discharge cycles), thus leading to a high energy density (57 W h kg^{-1}) and superior power density (17 kW kg^{-1}).

Introduction

Owing to the unique properties of high power density, rapid charging speed, ultralong cycle life and wide operating temperatures, carbon-based electrochemical double-layer capacitors (EDLCs) have attracted tremendous attention in many important applications, such as consumer electronics, electric vehicles or buses, uninterruptible power supplies, smart grids, and load-levelling equipment.[1–3] However, compared with batteries, the much lower energy densities (~6 W h kg^{-1}) of commercial EDLCs limit their application as a primary power source.[4]

The energy storage of EDLCs depends on the electrical double-layer adsorbed on the carbon electrode–electrolyte interface, and the energy density is proportional to their specific capacitance and operating voltage ($E = 1/2\ CV^2$).[5] Since the operating voltage is determined by the electrolytes/solvents, the specific capacitance of EDLCs plays a vital role in achieving high energy density. According to the charge storage mechanism of EDLCs, the capacitance is primarily dependent on the effective specific surface area (SSA) of carbon electrodes. In order to achieve high specific capacitance, carbon-based nanostructured materials, *e.g.* activated carbons,[6,7] mesoporous carbons,[8,9] carbide-derived carbons,[10,11] carbon nanotubes,[12,13] carbon fibers[14,15] and graphene,[16,17] have been explored as electrode materials for EDLCs. Among them, activated carbons (ACs), due to their high surface area, relatively low cost, great cycle stability, and easy production in large quantities, have been the most widely used electrode materials for commercial EDLCs.

Commercial activated carbons were commonly produced from valuable fossil fuels, such as petroleum coke, pitch and coal, leading to significant carbon/raw material weight loss and the release of serious toxic chemicals during the high-temperature pyrolysis (carbonization), thus causing waste of resources and environmental issues. In view of the above problems, in recent years lots of efforts have been devoted to the preparation of activated carbons from inexpensive biomass or biomass wastes, such as coconut shells,[18] durian shells,[19] rice brans,[20] pine cones,[21] beer lees,[22] bamboo fibers,[23] shiitake mushrooms,[24] hemp stems,[6] reed straw,[25] cotton,[26] cyanobacteria,[27] fungi,[28] shaddock peel,[29] willow leaves,[30] catkins[31] and pollens,[32] and SSAs of 1000–2500 m^2 g^{-1} can be reached. Although a SSA of 3000 m^2 g^{-1} was sometimes reported,[22] the useable SSA falls usually in the range of 1000–2000 m^2 g^{-1}, since some small micropores (<1 nm) are not easily accessible for electrolyte ions, particularly large organic or ionic liquid electrolyte ions (they can work at higher operating voltages, thus providing higher energy density). In order to achieve a high SSA and large portion

Laboratory of Solid State Ionics, School of Materials Science and Engineering, Huazhong University of Science and Technology, Wuhan 430074, P. R. China. E-mail: lwei@hust.edu.cn; xguo@hust.edu.cn; Fax: +86-27-87559804; Tel: +86-27-87559804

† The authors contributed equally to this work.

of mesopores, almost all the reported activated carbons from biomass precursors were synthesized by chemical activation in KOH, NaOH or $ZnCl_2$, *etc.* The obtained activated carbons almost present the morphology and structure of irregularly shaped fragments, with a narrow pore size distribution. In addition, post-processing, such as purification, is needed to remove metal ion impurities introduced by activation agents, and ball milling or grinding is generally necessary to lower the particle size. In order to increase the energy density of EDLCs and simultaneously decrease the production cost, it is highly demanded to choose appropriate carbon sources, develop novel synthesis methods and control the structure and porosity of activated carbon materials.

Spores, as one sort of microorganism, are a natural reservoir of carbon sources, and they are very inexpensive and widely available. The spore grains have a kind of core/shell structure. The core is filled with fragile sporoplasmic materials, such as cell sap, fat, nucleic acid, protein and polysaccharide. The protective shell is composed of two layers. The inner layer is called intine, which is made of delicate cellulose; the outer layer is called exine, which is constructed from extremely resilient sporopollenin, a highly cross-linked organic polymer of approximate composition $C_{90}H_{144}O_{27}$.[33] The sporopollenin exine is very stable both physically and chemically, being the sole bio-polymer to survive millions of years in sedimentary rocks.[34] Moreover, the exines of spores have a uniform morphology and structure, and there exist a large number of natural nanoscale channels (apertures) for mass transfer. Based on these properties, the sporopollenin exines of spores have attracted great attention as microcapsules for drug (and other actives) delivery, medical imaging and solid phase supports for peptide synthesis.[35,36] However, carbon materials derived from the spore exines for energy storage applications are seldom reported. The highly porous and hollow structure of spore exines combined with their small particle size and nanostructured surface sculptures would provide a large surface area and good transmission properties from both the outer and inner surfaces. How to convert the spores into activated carbons, and at the same time, retain the nano-architectures of spore exines during high-temperature carbonization and activation treatment, and how the unique morphologies and structures of the spore derived activated carbon electrodes influence the electrochemical performances of EDLCs are worthy of further research.

In this work, various spores, including *Lycopodium clavatum*, *Ganodorma lucidum* and *Lycopodium annotinum* spores were utilized as carbon sources, and the derived carbons were activated by CO_2. Compared with chemical activation, physical activation using CO_2 or steam as the activation agent does not need post-processing to remove metal ion impurities. More importantly, physical activation does not destroy the original morphology of spore exines. It is beneficial for activated carbon to maintain the featured nano-architecture of the spore exines with a high SSA and pore volume. As demonstrated here, after simple carbonization and CO_2 activation, various spore grains were transformed into activated carbon microspheres (ACMs) with 3D highly porous hierarchical architectures, and the nanostructured activated carbon electrodes showed high specific capacitance, very good rate capability and cycling stability for advanced EDLCs.

Experimental section

Three kinds of spores, including *Lycopodium clavatum*, *Ganodorma lucidum* and *Lycopodium annotinum* spores, are utilized as carbon precursors and self-templates. They are all edible and commercially available in large quantities. The preparation process of ACMs from spores mainly consists of three steps: pre-treatment, carbonization and activation, as shown in Scheme 1. The overall method is facile, green and sustainable, without using corrosive or toxic chemicals.

Pre-treatment of spores

10 g of spores were immersed into 50 mL of acetone with magnetic stirring for 6 hours, and then successively washed and filtered in ethanol and de-ionized water. This process could clean and remove the lipids on the surface of the spores. Then they were dried at 70 °C overnight in an oven. Afterwards, the resulting spores were heated at 300 °C in air for 6 h to burn the sporoplasm, delicate cellulose intine, and fix the special morphology of spore exine with the aid of oxygen. This process is very necessary to avoid the structural collapse in the following high-temperature carbonization.

Carbonization and activation

After pre-treatment, the obtained spore exines were transferred into a tube furnace for carbonization and activation. First, they were heated to 700 °C at a heating rate of 10 °C min^{-1} in an argon atmosphere, and maintained at this temperature for 2 h. After cooling down, black carbonized powders with relatively high conductivity were obtained. Next, the carbons were heated to 900 °C at a heating rate of 10 °C min^{-1} in an argon atmosphere, and then switched to a CO_2 atmosphere for activation for 6 h. Afterwards, the activated carbons were cooled down in an argon atmosphere again to minimize the possible formation

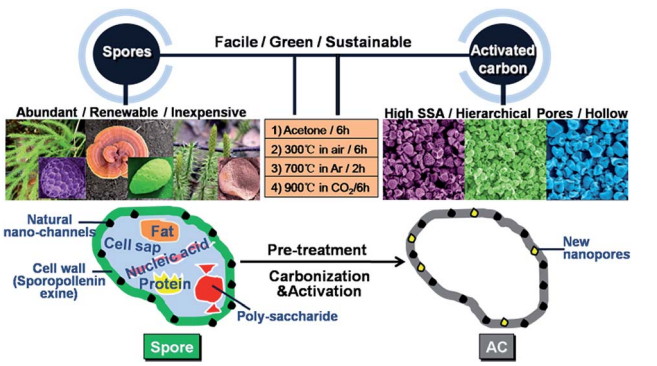

Scheme 1 Schematic illustration of the process to prepare hierarchical porous structured hollow microspheres of activated carbon from various spores (*Lycopodium clavatum*, *Ganodorma lucidum* and *Lycopodium annotinum*).

of surface groups at elevated temperature. This step could help opening, broadening and creating new pores, thus generating a porous structure with a high surface area.

Characterization

A field emission scanning electron microscope (FE-SEM, Sirion 200, FEI Corporation, Netherlands) and transmission electron microscope (TEM, Tecnai G2 20, FEI Corporation, Netherlands) were employed to observe the morphology, structure and particle size of the spores and spore-derived activated carbons. The surface area and pore size distribution of the samples were identified by N_2 adsorption–desorption tests using a surface area and porosity analyzer (ASAP 2020, Micromeritics Instrument Corporation, USA). The SSAs were calculated from N_2 adsorption isotherms using the Brunauer–Emmett–Teller (BET) equation based on the multi-molecular layer adsorption model, in the range of relative pressures (P/P_0) from 0.05 to 0.35. The pore size distributions were determined by the nonlocal density functional theory (NLDFT) analysis of N_2 adsorptions in carbon slit pores. The carbon structures of the materials were characterized by Raman spectra using a LabRAM HR800 spectrometer (HORIBA Jobin Yvon Corporation, France) with a Nd:YAG laser at an excitation wavelength of 532 nm and a power of 50 mW, and an X-ray diffractometer (XRD, X'Pert PRO, PANalytical B. V., Netherlands) with a 3 kW ceramic tube as the X-ray source and an X'celerator detector. Moreover, the elemental and surface chemical compositions of the samples were identified by X-ray photoelectron spectra (XPS) collected on an AXIS Ultra DLD-600W spectrometer (Kratos Corporation, Japan) with a monochromatic Al Kα X-ray source. The electrical conductivities of the activated carbon electrodes were measured using a four probe setup (Keithley 4200-SCS, Keithley Instruments Inc., USA).

Fabrication of EDLCs and electrochemical measurements

To prepare the electrodes, activated carbons and polytetrafluoroethylene (PTFE) with a weight ratio of 92 : 8 were mixed in ethanol on a hotplate with magnetic stirring, until the powders became a gum-like composite. Then the composite was rolled and cut into rounds (12 mm in diameter and 120–150 μm in thickness) for EDLC electrodes. Next, the electrodes were dried in the transition chamber of a glovebox at 120 °C under vacuum overnight to remove the moisture and residual hydrocarbons. Then they were transferred into the glovebox directly without exposing to air for weighing and paring. The symmetric coin cell type EDLCs were constructed by using two activated carbon electrodes with the same mass separated by using a cellulose separator (TF4030, NKK, Japan). Aluminum foil (0.3 mm in thickness) coated with conductive graphite (10–20 μm) was attached to each electrode as the current collector. The graphite coating was applied to reduce the interfacial resistance between the electrode and the Al current collector. 1 M tetraethylammonium tetrafluoroborate ($TEABF_4$, 99%, Alfa Aesar) dissolved in acetonitrile solution (AN, 99.8+%, Alfa Aesar) was used as the electrolyte due to its application in most commercial supercapacitors.

All the electrochemical measurements were performed at room temperature. Cyclic voltammetry (CV) tests were performed in the voltage range of 0–2.3 V at scan rates of 1–500 mV s^{-1} by using a CHI660E electrochemical workstation (CH Instruments, Inc.). The carbon gravimetric capacitance, C (F g^{-1}), was calculated according to the following equation:

$$C = \frac{2I}{(\mathrm{d}V/\mathrm{d}t)m} \quad (1)$$

where I is the current (A), $\mathrm{d}V/\mathrm{d}t$ is the scan rate (V s^{-1}), and m is the active mass of a single carbon electrode (g).

Electrochemical impedance spectroscopy (EIS) was performed in the frequency range of 1 mHz to 100 kHz at open circuit potential with an AC amplitude of 10 mV by employing a Solartron 1296A impedance analyzer (Solartron Analytical, UK). The carbon gravimetric capacitance, C (F g^{-1}), was calculated according to the following equation:

$$C = \frac{2|\mathrm{Im}(Z)|}{2\pi f\left[\left(\mathrm{Im}(Z)\right)^2 + \left(\mathrm{Re}(Z)\right)^2\right]m} \quad (2)$$

where f is the operating frequency (Hz), $\mathrm{Im}(Z)$ and $\mathrm{Re}(Z)$ are the imaginary and real parts of the total device resistance (Ohm), and m is the active mass of a single carbon electrode (g).

The galvanostatic charge–discharge properties of EDLCs were also evaluated using a CHI660E electrochemical workstation in the voltage range of 0–2.3 V at current densities between 0.1 and 20 A g^{-1}. A charge–discharge test of 10 000 cycles was implemented by using a LANHE CT2001A charge–discharge system (Wuhan LAND Electronics Co., Ltd.) at a constant current density of 2 A g^{-1}. The carbon gravimetric capacitance, C (F g^{-1}), was calculated according to the following equation:

$$C = \frac{2I}{(\mathrm{d}V/\mathrm{d}t)m} \quad (3)$$

where I is the current (A), $\mathrm{d}V/\mathrm{d}t$ is the slope of the discharge curve (V s^{-1}), and m is the active mass of a single carbon electrode (g).

The energy density, E_{cell} (W h kg^{-1}) and power density, P (W kg^{-1}) of EDLCs were estimated from equations (4) and (5), respectively:

$$E_{\mathrm{cell}} = \frac{1}{8}CV^2 \quad (4)$$

$$P = \frac{E_{\mathrm{cell}}}{t} \quad (5)$$

where C is the carbon gravimetric capacitance (F g^{-1}), V is the operating potential (V), and t is the discharge time (h).

Results and discussion

The SEM images of the original *Lycopodium clavatum*, *Ganodorma lucidum* and *Lycopodium annotinum* spore grains, and the finally obtained activated carbons are shown in Fig. 1–3. After carbonization and activation, the activated carbon samples retain the original skeleton morphology of the spore exines, presenting a porous hollow spherical structure on a micrometer

scale. The TEM images of the spore-derived activated carbons at different magnifications are presented in Fig. 4. Among them, *Lycopodium clavatum* spore derived activated carbon microspheres (ACM-LC) are approximately 10–15 μm in diameter with a hemispherical cap ending in the trilete structure on the underside (Fig. 1b and 4a). The particle size of ACM-LC is smaller than that of the original spores (~25 μm in diameter, Fig. 1a), due to the loss of the support of the core substances during the heat-treatment processes, resulting in the shrinkage of the volume. The surface sculptures of the spherical shell are constructed by reticulate microridges and continuous with large porous walls as well as nano-sized channels (Fig. 1c and 4b). The shell thickness is ~1 μm (Fig. 1d). From Fig. 2, it can be seen that *Ganodorma lucidum* spore derived activated carbon microspheres (ACM-GL) have an ellipsoidal morphology with a diameter of 3–4 μm in the major axis (Fig. 2b and 4c). The surface of ACM-GL presents a continuous porous network with

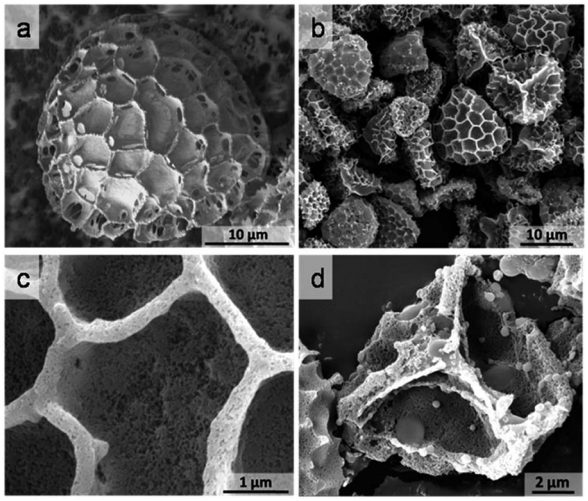

Fig. 1 (a) SEM image of the original *Lycopodium clavatum* spore grain and (b–d) SEM images of ACM-LC.

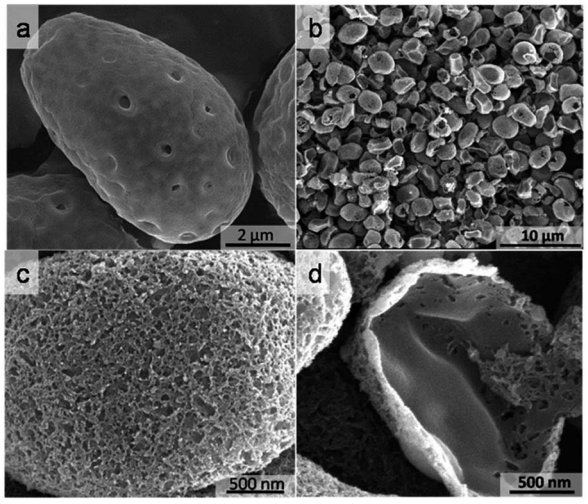

Fig. 2 (a) SEM image of the original *Ganodorma lucidum* spore grain and (b–d) SEM images of ACM-GL.

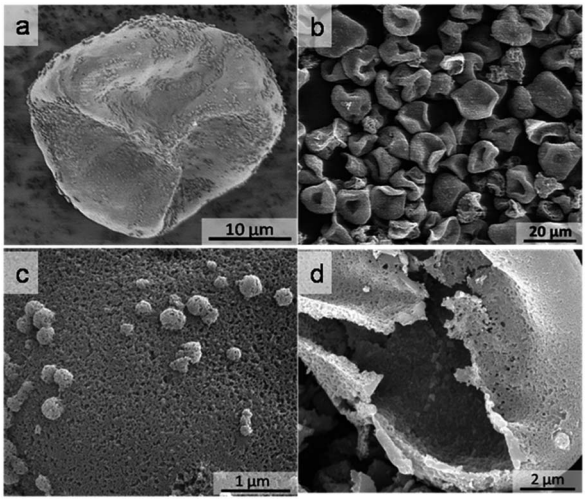

Fig. 3 (a) SEM image of the original *Lycopodium annotinum* spore grain and (b–d) SEM images of ACM-LA.

nanoscale apertures (Fig. 2c and 4d). The shell thickness of ACM-GL is only 100–200 nm (Fig. 2d and 4d). *Lycopodium annotinum* spore derived activated carbon microspheres

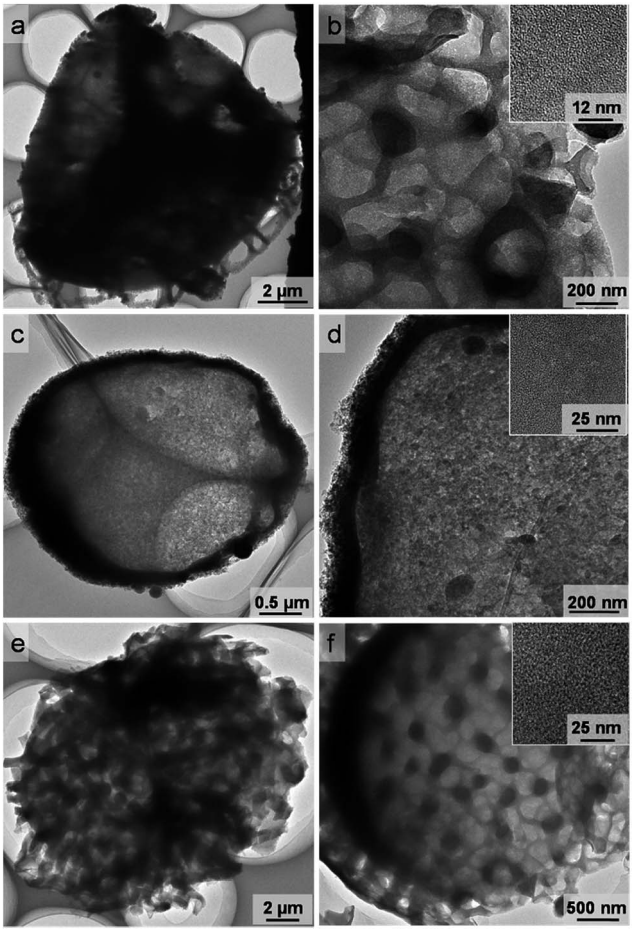

Fig. 4 TEM images of ACMs derived from several spores at different magnifications: (a and b) ACM-LC, (c and d) ACM-GL, and (e and f) ACM-LA.

(ACM-LA) have a tetrahedral morphology and the particle size is about 15 μm (Fig. 3b and 4e). The surface of ACM-LA also presents a porous structure but with tuberculate nanoparticle ornamentations (Fig. 3c and 4f). The shell thickness of ACM-LA is about 500 nm (Fig. 3d). Compared with *Lycopodium clavatum* spores, *Ganodorma lucidum* and *Lycopodium annotinum* spores have thinner exines, and therefore, after carbonization and activation the obtained ACM-GL and ACM-LA possess thinner spherical shells. They are more prone to deformation, and even break owing to the burning off of the core substances, as shown in Fig. 2b and 3b.

Raman spectra of the spore derived ACMs revealed the microstructure of the produced carbon materials (Fig. 5). All the samples show similar characteristics with a G-band located at ~1590 cm^{-1} and a D-band located at ~1340 cm^{-1}. The G-band corresponds to the graphite structure, *i.e.* the E_{2g} in-plane optical mode of graphene.[37] The D-band is associated with the double-resonance Raman process in disordered carbons.[38] The intensity of the D-band depends on the disorder and defects in the carbon structures. The high ratio of the intensities of the two peaks ($I_D/I_G = 1.13$) indicates large defects existing in the ACMs as well as a high content of amorphous carbon.[39]

XRD measurements (Fig. 6) further demonstrate the structural characterization of the produced ACMs. Activated carbons generally show a (002) diffraction peak at $2\theta \sim 25°$ and overlapped (100) and (101) peaks (usually identified as the (10) peak) at $2\theta \sim 42°$.[40] It can be seen that after CO_2 activation, the spore derived ACMs show a well-developed graphitic stacking peak at 2θ of 26.2–26.5° and a broad weak peak at 2θ of 42.4–42.9° due to the formation of a high degree of interlayer condensation.[41] The more pronounced peaks of the sample ACM-LC at 26.5° and 42.9°, compared with those of the samples ACM-GL and ACM-LA, indicate the improved electrical conductivity of ACM-LC.

The electrical conductivities of the ACM electrodes (92% ACMs + 8% PTFE) and commercial activated carbon electrodes (92% TF-B520 + 8% PTFE) were measured using a four probe setup and were found to be 55.6 mS cm^{-1} for ACM-LC, 24.8 mS cm^{-1} for ACM-GL, 22.6 mS cm^{-1} for ACM-LA, and 15.76 mS cm^{-1} for TF-B520. Compared with the conductivities of commercial activated carbons and the bio-carbons reported in the literatures (0.62–38 mS cm^{-1}),[42–45] the conductivity of the ACM-LC sample is clearly higher, and thus it could contribute to achieve large capacitance and great rate capability.

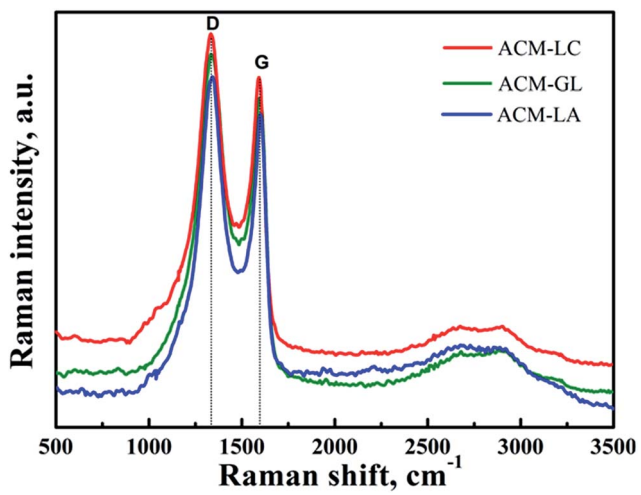

Fig. 5 Raman spectra of ACMs derived from several spores.

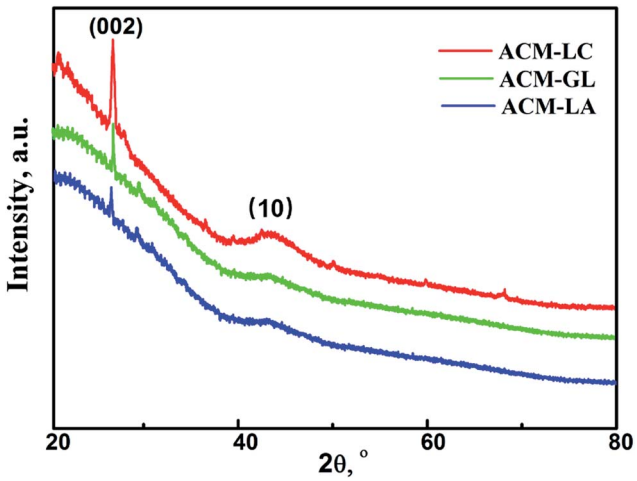

Fig. 6 XRD patterns of ACMs derived from several spores.

The XPS spectra further assist in understanding the elemental composition and surface chemical composition of the prepared ACMs (Fig. 7). After activation, there are C, O and N elements detected in these samples (Fig. 7a). The high-resolution C 1s spectra (Fig. 7b) exhibit strong sp^2 peaks (C–C) located around 284.8 eV, and no obvious oxygen-containing functional groups are present after 900 °C heat-treatment. The O 1s peaks located at ~232.6 eV are mainly attributed to the small quantity of adsorbed water molecules (H–O–H) on the surface of our samples.[46] The atomic fractions of O in the samples are only 2–4 at%. Moreover, from the high-resolution N 1s spectra (Fig. 7c), we can see that the deconvoluted N 1s spectra contain three characteristic peaks at binding energies around 398.7, 401 and 403.6 eV, corresponding to the pyridinic N, graphitic N and pyridinic N^+–O^- groups,[47,48] respectively. However, the atomic percentages of N in the ACMs are very low, only 0.22 at% for ACM-LC, 0.31 at% for ACM-GL and 0.37 at% for ACM-LA. The above results demonstrate the high purity of our carbon materials.

In order to investigate the SSA and pore structural properties of the prepared ACMs, nitrogen sorption (BET) measurements were carried out, and the results are shown in Fig. 8. According to the classification of the International Union of Pure and Applied Chemistry (IUPAC), all the samples exhibit type IV isotherms[49] with a continuous slope above a relative pressure (P/P_0) of 0.2, and a hysteresis loop in the relative pressure range between 0.45 and 0.99 (Fig. 8a). This phenomenon suggests the existence of mesopores, and even macropores in the ACMs. The BET SSA and pore volume of ACMs are summarized in Table 1. In accordance with the variation of the N_2 adsorption amounts in Fig. 8a, among the three samples, ACM-LC exhibits the highest SSA, which is up to 3053 m^2 g^{-1}, and the total pore volume is up to 1.43 cm^3 g^{-1}. The NLDFT pore size distributions

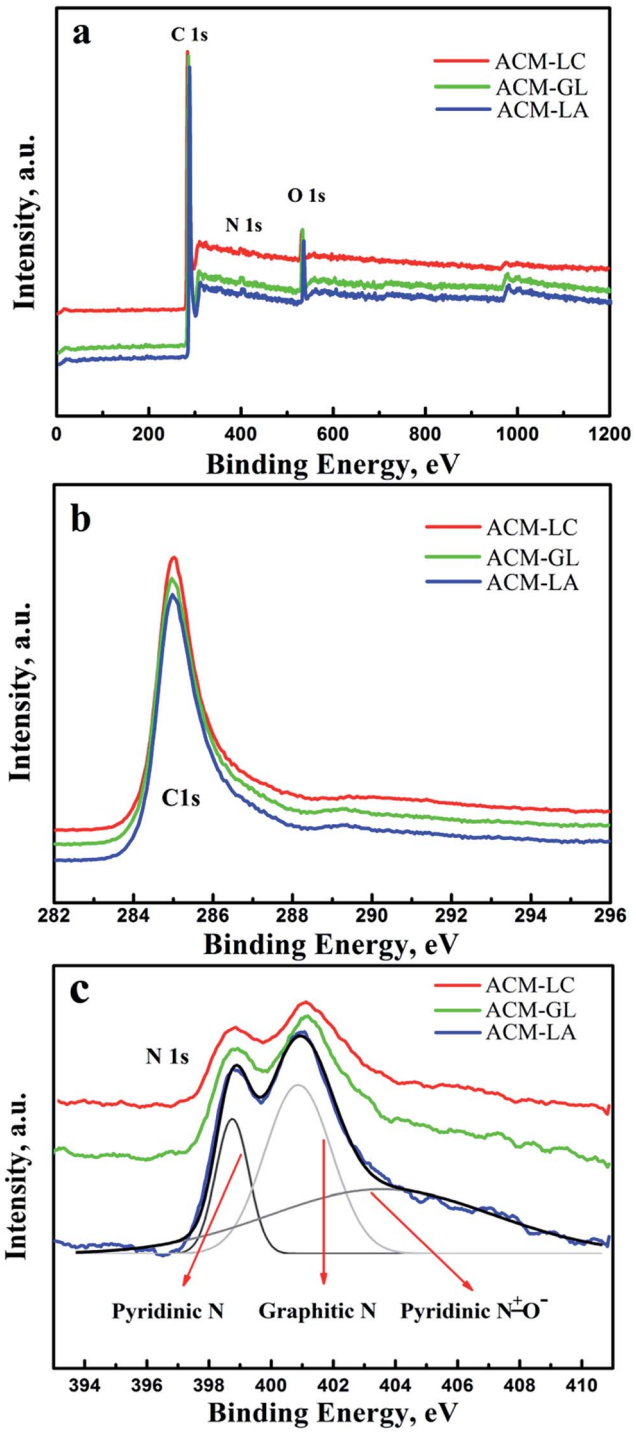

Fig. 7 (a) XPS spectra of ACMs derived from several spores, (b) high-resolution C 1s spectra and (c) high-resolution N 1s spectra.

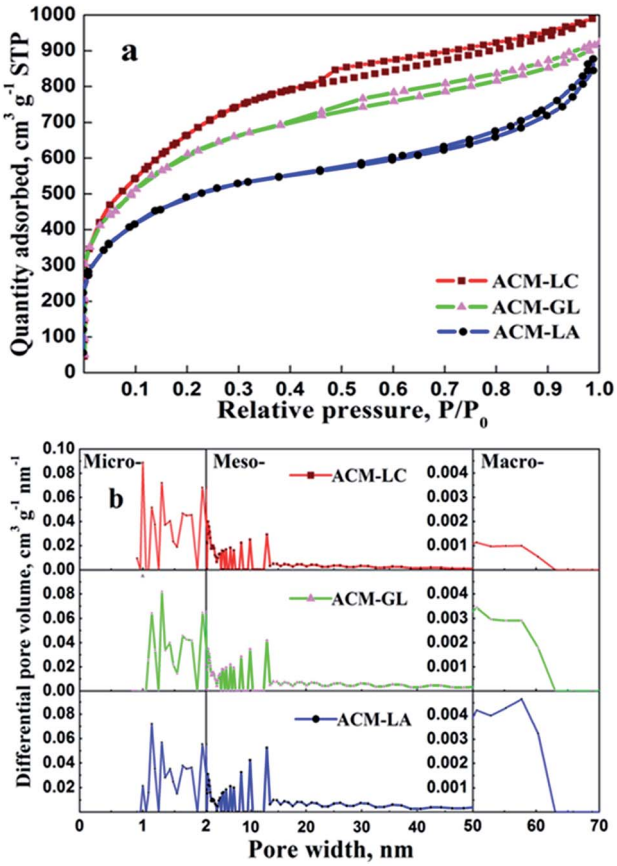

Fig. 8 (a) N_2 adsorption/desorption isotherms and (b) pore size distribution curves calculated by using an NLDFT model on carbon slit pores for ACMs derived from several spores.

of ACMs are shown in Fig. 8b. It can be seen that all the samples exhibit a hierarchical porous structure (Scheme 2) with a pore size distribution mainly in the range of 1–65 nm. The meso-/macropores in the spherical shell combined with the conductive carbon wall could provide fast ionic transportation, and the micropores could provide a high SSA for the adsorption/desorption of electrolyte ions. Although macropores (>50 nm) are beneficial to the permeation and diffusion of electrolyte ions into the activated carbon electrodes,[50] a high content of macropores will decrease the SSA of activated carbon materials, and thus reduce the specific capacitance and energy density of EDLCs. In our samples, the content of macropores is very low (only 0.01–0.06 $cm^3\ g^{-1}$, Table 1), and micropores and mesopores occupy the most proportions. In particular, the ACM-LC sample has the largest volume of micropores (0.83 $cm^3\ g^{-1}$) compared with the other two samples, thus displaying a relatively high SSA.

The electrochemical performances of EDLCs with ACMs as electrodes were investigated in 1 M $TEABF_4$/AN electrolyte, which is the most popular organic electrolyte for commercial supercapacitors. Fig. 9a–c show the CV curves of the ACM electrodes. At a low scan rate of 2 mV s^{-1}, all the samples show CV curves in a symmetrical rectangular shape without obvious faradaic peaks, which is the characteristic of almost ideal EDLCs. Among the three samples, ACM-LC electrodes present the biggest rectangular area at a scan rate of 2 mV s^{-1}, meaning that ACM-LC has the highest specific capacitance, which is in accordance with its largest SSA. With increasing scan rates, the shapes of CV curves distort gradually, which is common for EDLCs. However, when the scan rate increases to 100 mV s^{-1}, only the samples ACM-GL and ACM-LA retain the rectangular shape. This phenomenon indicates that ACM-GL and ACM-LA have quicker ion transportation ability at high scan rates, which

Table 1 SSA and pore volume of ACMs derived from several spores

Sample	BET SSA ($m^2\ g^{-1}$)	Pore volume ($cm^3\ g^{-1}$)	Micropore volume ($cm^3\ g^{-1}$)	Mesopore volume ($cm^3\ g^{-1}$)	Macropore volume ($cm^3\ g^{-1}$)
ACM-LC	3053	1.43	0.83	0.59	0.01
ACM-GL	2401	1.42	0.75	0.64	0.03
ACM-LA	1693	1.35	0.67	0.62	0.06

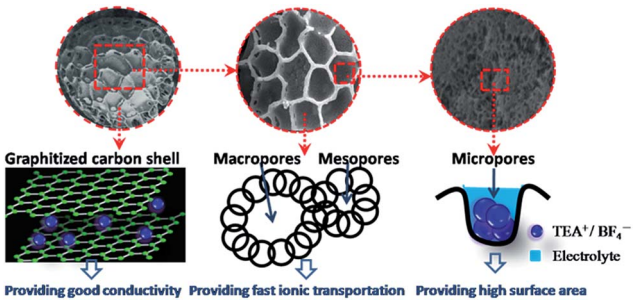

Scheme 2 Schematic illustration of the structural properties of the microspheres of activated carbon from spores.

is attributed to their thinner spherical shells (Fig. 2d and 3d), and the larger volume of meso-/macropores in the shells (Table 1). The influence of scan rates on the specific capacitances of ACMs is summarized in Fig. 9d. The highest specific capacitances of the three ACMs reach 308 F g^{-1} (81.74 F cm^{-3}, ACM-LC), 262 F g^{-1} (64.88 F cm^{-3}, ACM-GL) and 171 F g^{-1} (43.85 F cm^{-3}, ACM-LA). When the scan rate increases to a very high value of 500 mV s^{-1}, the capacitances still remain at 164 F g^{-1} (54%), 124 F g^{-1} (47%) and 90 F g^{-1} (53%), respectively. Although ACM-GL and ACM-LA have larger meso-/macropore proportions compared with that of ACM-LC, they present similar capacitance retention (~50%) at a scan rate of 500 mV s^{-1}. Owing to ultrahigh scan rates, the adsorption of electrolyte ions almost occurs on the external surfaces of the electrodes, and they can hardly transport into the nano-channels of the porous electrodes. Moreover, compared with the capacitance of commercial activated carbon for supercapacitors (TF-B520) at a scan rate of 500 mV s^{-1} (25 F g^{-1}, Fig. 9d), ACM-LC exhibits a six times higher specific capacitance value.

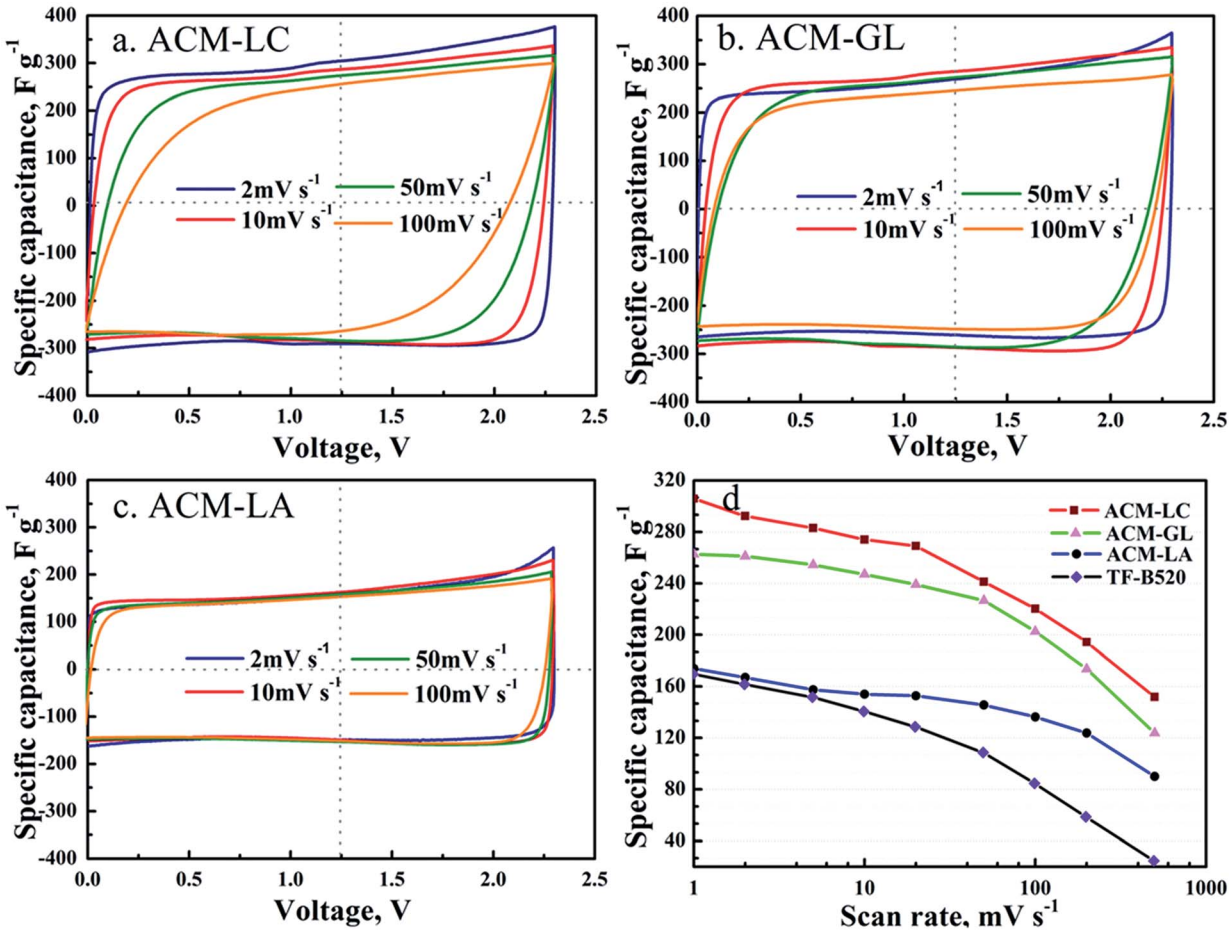

Fig. 9 Electrochemical characterization of ACMs derived from various spores in 1 M $TEABF_4$/AN electrolyte: (a–c) cyclic voltammograms and (d) specific capacitances of the ACMs as a function of the scan rate, with commercial activated carbon TF-B520 for comparison.

The much faster ionic transportation rate and high capacitance retention of ACM-LC at ultrafast scan rates should be related to their relatively high conductivity, reticulate microridge sculptures on the surface (Fig. 1c) and the hollow structure (Fig. 1d). These features provide a large external surface area, and could assist the electrolyte ions in transporting through the inner and outer surfaces of the spherical shells simultaneously, thus making the full utilization of the entire material for charging and discharging.

The electrochemical impedance behaviors of the ACM electrodes in 1 M $TEABF_4$/AN electrolyte are presented in Fig. 10a. The Nyquist plots of all samples exhibit the typical features of porous electrodes with a 45° Warburg region at high to medium frequencies, and an almost vertical line at low frequencies.[51] At

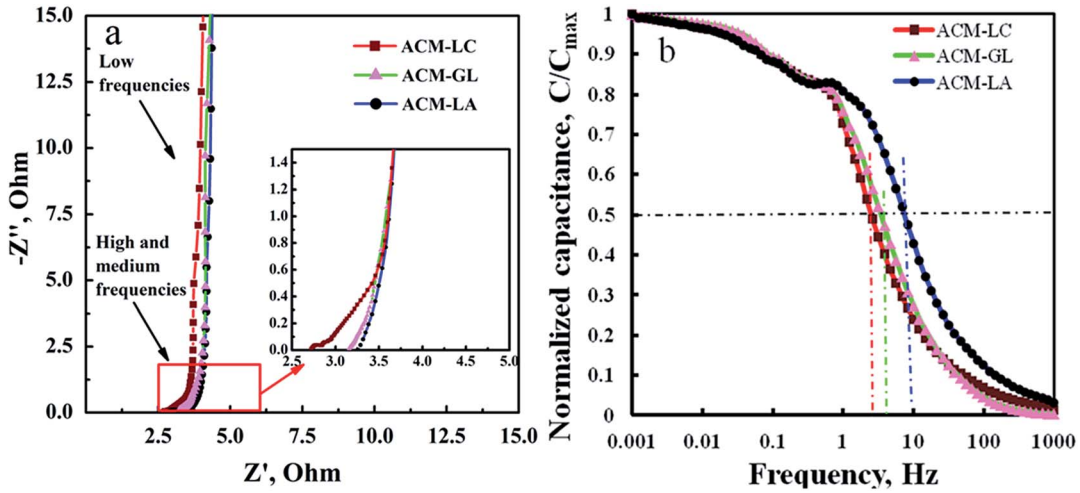

Fig. 10 Electrochemical characterization of ACMs derived from various spores in 1 M $TEABF_4$/AN electrolyte: (a) Nyquist plots and (b) the frequency response.

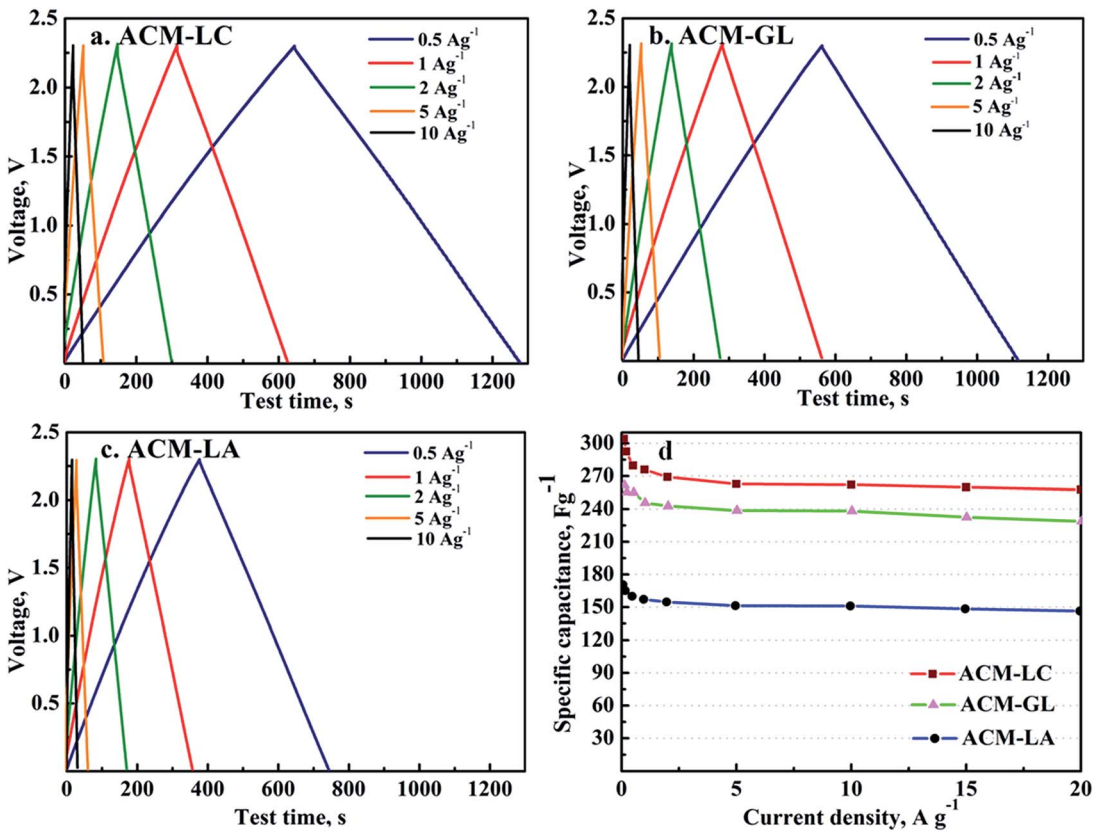

Fig. 11 Electrochemical characterization of ACMs derived from various spores in 1 M $TEABF_4$/AN electrolyte: (a–c) galvanostatic charge–discharge curves, and (d) specific capacitances as a function of current densities from 0.1 A g^{-1} to 20 A g^{-1}.

high-medium frequencies, the length of the 45° Warburg region is related to the ion diffusion/transport process from the electrolyte into the carbon pores. Among all the samples, ACM-LC shows an apparently longer 45° Warburg segment, which indicates an increased resistance (Warburg resistance) faced by the electrolyte ions during their transport through the surface of the spherical shell into the inner micropores. This result is in accordance with the transformation of CV curves (Fig. 9a). ACM-LC has the highest content of micropores (Table 1). The existence of micropores is critical for achieving high capacitance values in both aqueous and organic electrolytes, due to the distortion of solvation shells and closer approach of the ions to the pore walls.[52,53] However, the appearance of meso-/macropores is beneficial for the fast diffusion of large ions in organic electrolytes. The ACM-LA sample has the largest meso-/macropore volume (Table 1), and thus presents the shortest 45° Warburg segment and the smallest Warburg resistance.

The complementary information from EIS about the frequency response of ACMs in EDLCs is presented in Fig. 10b. The capacitances of all the samples show saturation at a frequency below ~0.7 Hz, suggesting that near equilibrium ion adsorption could be achieved within seconds. If we approximate the highest operating frequency as the frequency at which the capacitance drops to half of its maximum value ($C/C_{max} = 0.5$), it can be seen that the ACMs display an ultrafast frequency response with frequency values from 2.6 to 10 Hz. These values are apparently high, and even an order of magnitude higher than those of other reported carbon materials.[6,21,23,25,27,30,31] The great frequency responses of ACMs from spores make them very attractive for applications in ultrahigh power EDLCs.

The performance of EDLCs in real applications is primarily determined by their charge–discharge (C–D) characteristics, which reveal their energy and power performances. Fig. 11 shows the galvanostatic C–D properties at different current

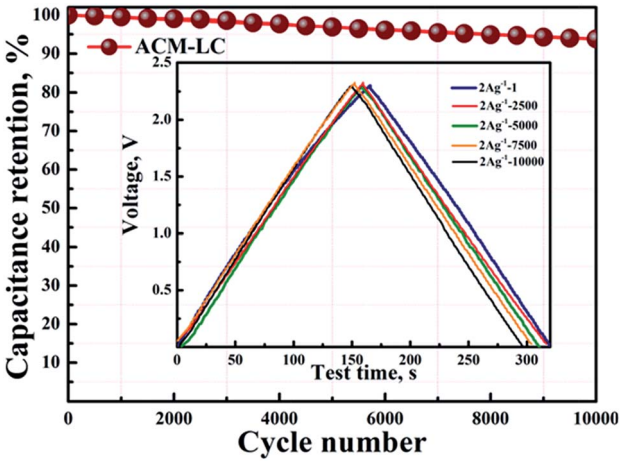

Fig. 12 Cycling stability of an EDLC based on ACM-LC electrodes in 1 M $TEABF_4$/AN electrolyte tested at a current density of 2 A g^{-1}. The inset is the charge–discharge curves of the cell at every 2500 cycles.

Table 2 Activated carbons from bio-materials for supercapacitors

Bio-material	Activation	Nitrogen doped	Metal oxide composited	Electrolyte	SSA (m^2 g^{-1})	Capacitance (F g^{-1})	Reference
L. clavatum spores	CO_2	—	—	1 M $TEABF_4$ in AN	3053	305	This work
Hemp stems	KOH	—	—	1.8 M $TEABF_4$ in PC	2879	160	6
Durian shells	H_3PO_4	—	—	1.5 M Na_2SO_4	2004	93.1	19
Rice brans	NaOH	—	—	6 M KOH	2475	265	20
Pine cones	KOH	—	—	1 M Na_2SO_4	1515	137	21
Beer leers	KOH	—	—	0.1 M H_2SO_4	3560	188	22
Bamboo	Ta–Ni–Fe–Zn–Cl–F	—	—	6 M KOH	—	136	23
Shiitake mushroom	H_3PO_4	—	—	6 M KOH/($TEABF_4$/AN)	2988	306/149	24
Reed straw	KOH	✓	—	6 M KOH	2497	297	25
Cotton	KOH	—	—	KOH	2436	283	26
Pyrolytic cyanobacteria	KOH	—	—	6 M KOH	2184	271	27
Willow leaves	$ZnCl_2$	—	—	6 M KOH	1031	216	30
Willow catkins	KOH	—	—	6 M KOH	997	306	31
Lotus pollens	CO_2	—	—	1 M H_2SO_4	2566	244	32
Silk	—	✓	—	$EMIMBF_4$	2494	242	54
Chitosan	KOH	✓	—	6 M KOH	2435	197	55
Bamboo	KOH	✓	—	6 M KOH	1472	301	56
Paulownia flower	KOH	✓	—	1 M H_2SO_4	1471	297	57
Bacterial cellulose	Polyaniline	✓	@MnO_2	1 M Na_2SO_4	1326	273	58
Cotton	—	✓	—	1 M H_2SO_4	1085	207	59
Surplus sludge	—	✓	—	1 M H_2SO_4	940	247	60
Bacterial cellulose	H_3PO_4, $NH_4H_2PO_4$, H_3BO_3/H_3PO_4	✓	—	2 M H_2SO_4	289	205	61
Cotton	$KMnO_4$	—	@MnO_2	0.5 M Na_2SO_4	35.6	128	64
Bacillus subtilis bacteria	—	—	@NiO	6 M KOH	49	343	65
Sawdust	—	—	@Co_3O_4	6 M KOH	—	290	66
Bacterial cellulose	—	✓	@MnO_2	1 M Na_2SO_4	252	256	67

densities for all the samples. From the voltage profiles at typical current densities (Fig. 11a–c), we can see that the C–D curves of the ACM electrodes are ideally symmetrical, and show a good time–potential linear relationship even at high current densities. At a low current density of 0.1 A g^{-1}, ACM-LC presents the highest specific capacitance of 305 F g^{-1} (Fig. 11d). With increasing current loads, the capacitance decreases gradually. The reduction of capacitance is generally attributed to the resistance of electrolyte ions travelling in the nanopores and interacting with the carbon defects revealed by the Raman spectra (Fig. 5). However, when the current load increases to a very high value up to 20 A g^{-1}, ACM-LC still holds a high capacitance of 263 F g^{-1}. The large capacitance combined with the great rate capability of ACM-LC is in accordance with the results of CV and EIS measurements. Compared with the other activated carbons from bio-materials in organic electrolytes recently reported in the literature, it is significantly advanced and even exceeding the great majority of N-doped[54–62] or metal oxide composited[63–66] activated carbons in aqueous electrolytes (they will produce extra pseudocapacitance), as listed in Table 2. Moreover, ACM-GL and ACM-LA also present superior capacitance retention at high current densities (Fig. 11d), however, the relatively low SSAs limit their maximum capacitance storage capabilities.

To investigate the long time stability of the ACM electrodes, a C–D test of 10 000 cycles was carried out on the optimal sample ACM-LC at a current density of 2 A g^{-1} (Fig. 12), which represents a current load for high-power application. The inset is the C–D curves of the ACM electrodes at every 2500 cycles. During the long time cycles, the shapes of the C–D curves are still linear with no overt IR-drops, as expected for nearly ideal capacitors. After 10 000 cycles, the capacity retention of the ACM-LC electrodes reaches 93.8%, indicating an outstanding cycling stability of the ACM electrodes. The energy and power densities (Ragone plot) calculated from the C–D tests for the EDLC with ACM-LC electrodes in 1 M $TEABF_4$/AN electrolyte are given in Fig. 13a. The cell exhibits the highest energy density of 56 W h kg^{-1} at a power density of 60 W kg^{-1}, and still maintains 47.7 W h kg^{-1} at a super-high power density of 17 kW kg^{-1}. The capacitance performances of the ACMs from various spores are summarized in Fig. 13b. Compared with other carbon materials, such as activated carbons,[6,19,21,24,25,32,59,67,68] carbon aerogels,[69–71] carbon fibers,[72–74] carbon nanotubes[75–79] and graphenes,[71,80–84] the ACMs from spores, due to their high SSA and hierarchical porous structure, can achieve excellent specific capacitance in organic electrolytes, and deliver a high energy density combined with excellent power density, which are superior to those of the great majority of the carbon-based supercapacitors.

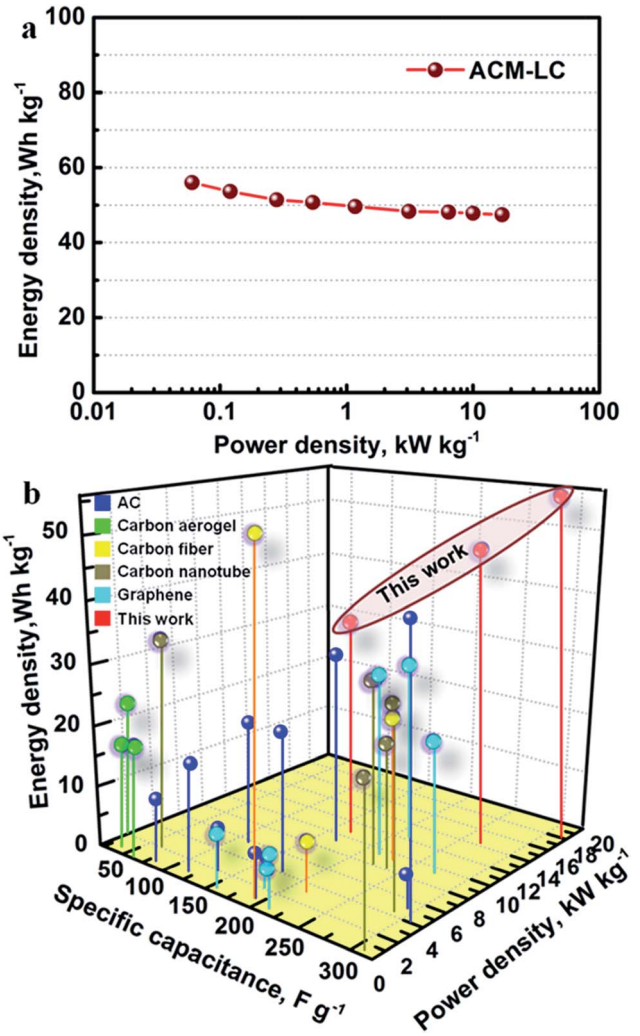

Fig. 13 (a) Ragone plot of the EDLC based on ACM-LC electrodes in 1 M $TEABF_4$/AN electrolyte, and (b) the summary of the capacitance performances of ACMs from spores, with other carbon materials reported in the literature for comparison.

Conclusions

We have successfully developed a facile, sustainable and low-cost route to produce highly porous hollow microspheres of activated carbon directly from natural spores (*Lycopodium clavatum*, *Ganodorma lucidum* and *Lycopodium annotinum* spores). These ACMs retained the favorable 3D nano-architectures of the spore exines, exhibiting a high SSA and hierarchical porous structure, which allow for superior electrical double-layer storage performances. Among all the samples, *Lycopodium clavatum* spore derived activated carbon microspheres (ACM-LC) present the highest SSA (3053 m^2 g^{-1}) due to the individual reticulate microridge structure on the surface of the spherical shell, optimal pore size distribution (large proportion of micropores combined with moderate meso-/macropores), and the highest electrical conductivity. These features contribute to achieve high capacitance and simultaneously facilitate the fast transportation of electrolyte ions into the carbon electrodes. As a result, the EDLC based on ACM-LC electrodes in organic electrolyte shows the highest specific capacitance (308 F g^{-1} and 81.74 F cm^{-3}), excellent rate capability (retaining 263 F g^{-1} at a superhigh current density of 20 A g^{-1}) and good cyclability (93.8% retention after 10 000 cycles). Moreover, owing to the green, facile and easy mass production nature of the synthesis

procedure, the activated carbon materials have great potential as practical electrode materials for ultrafast high energy EDLCs.

Acknowledgements

This work was supported by the National Natural Science Foundation of China (51502105).

References

1 P. Simon and Y. Gogotsi, *Nat. Mater.*, 2008, **7**, 845–854.
2 A. S. Aricò, P. Bruce, B. Scrosati, J.-M. Tarascon and W. Van Schalkwijk, *Nat. Mater.*, 2005, **4**, 366–377.
3 J. R. Miller and P. Simon, *Science*, 2008, **321**, 651–652.
4 L. Zhang, F. Zhang, X. Yang, K. Leng, Y. Huang and Y. S. Chen, *Small*, 2013, **9**, 1342–1347.
5 Q. Wang, J. Yan and Z. J. Fan, *Energy Environ. Sci.*, 2016, **9**, 729–762.
6 W. Sun, S. M. Lipka, C. Swartz, D. Williams and F. Q. Yang, *Carbon*, 2016, **103**, 181–192.
7 Q. X. Xie, R. R. Bao, A. R. Zheng, Y. F. Zhang, S. H. Wu, C. Xie and P. Zhao, *ACS Sustainable Chem. Eng.*, 2016, **4**, 1422–1430.
8 B. Liu, H. Q. Yao, R. A. Daniels, W. Q. Song, H. Q. Zheng, L. Jin, S. L. Suib and J. He, *Nanoscale*, 2016, **8**, 5441–5445.
9 T. Q. Lin, I. W. Chen, F. X. Liu, C. Y. Yang, H. Bi, F. F. Xu and F. Q. Huang, *Science*, 2015, **350**, 1508–1513.
10 J. Chmiola, C. Largeot, P. L. Taberna, P. Simon and Y. Gogotsi, *Science*, 2010, **328**, 480–483.
11 M. Oschatz, P. Pre, S. Dorfler, W. Nickel, P. Beaunier, J. N. Rouzaud, C. Fischer, E. Brunner and S. Kaskel, *Carbon*, 2016, **105**, 314–322.
12 B. Lee, C. Lee, T. Liu, K. Eom, Z. Chen, S. Noda, T. F. Fuller, H. D. Jang and S. W. Lee, *Nanoscale*, 2016, **8**, 12330–12338.
13 K. Shi, M. Ren and I. Zhitomirsky, *ACS Sustainable Chem. Eng.*, 2014, **2**, 1289–1298.
14 W. N. Xu, S. G. Dai, G. L. Liu, Y. Xi, C. G. Hu and X. Wang, *Electrochim. Acta*, 2016, **203**, 1–8.
15 G. Nagaraju, Y. H. Ko, S. M. Cha, S. H. Im and J. S. Yu, *Nano Res.*, 2016, **9**, 1507–1522.
16 H. Li, Y. Tao, X. Y. Zheng, Z. J. Li, D. H. Liu, Z. Xu, C. Luo, J. Y. Luo, F. Y. Kang and Q. H. Yang, *Nanoscale*, 2015, **7**, 18459–18463.
17 Y. Zhang, B. L. Tao, W. Xing, L. Zhang, Q. Z. Xue and Z. F. Yan, *Nanoscale*, 2016, **8**, 7889–7898.
18 B. Kishore, D. Shanmughasundaram, T. R. Penki and N. Munichandraiah, *J. Appl. Electrochem.*, 2014, **44**, 903–916.
19 J. Tey, M. Careem, M. Yarmo and A. Arof, *Ionics*, 2016, **22**, 1209–1216.
20 J. Hou, C. Cao, X. Ma, F. Idrees, B. Xu, X. Hao and W. Lin, *Sci. Rep.*, 2014, **4**, 7260.
21 A. Bello, N. Manyala, F. Barzegar, A. A. Khaleed, D. Y. Momodu and J. K. Dangbegnon, *RSC Adv.*, 2016, **6**, 1800–1809.
22 S. G. Lee, K. H. Park, W. G. Shim, M. S. Balatnanigaimani and H. Moon, *J. Ind. Eng. Chem.*, 2011, **17**, 450–454.
23 X. Y. Tao, J. Du, Y. P. Li, Y. C. Yang, Z. Fan, Y. P. Gan, H. Huang, W. K. Zhang, L. X. Dong and X. D. Li, *Adv. Energy Mater.*, 2011, **1**, 534–539.
24 P. Cheng, S. Y. Gao, P. Y. Zang, X. F. Yang, Y. L. Bai, H. Xu, Z. H. Liu and Z. B. Lei, *Carbon*, 2015, **93**, 315–324.
25 Q. X. Xie, A. R. Zheng, S. B. Zhai, S. H. Wu, C. Xie, Y. F. Zhang and Y. F. Guan, *J. Solid State Electrochem.*, 2016, **20**, 449–457.
26 P. Cheng, T. Li, H. Yu, L. Zhi, Z. H. Liu and Z. B. Lei, *J. Phys. Chem. C*, 2016, **120**, 2079–2086.
27 K. L. Wang, Y. H. Cao, X. M. Wang, Q. H. Fan, W. Gibbons, T. Johnson, B. Luo and Z. R. Gu, *Energy*, 2016, **94**, 666–671.
28 C. Long, X. Chen, L. Jiang, L. Zhi and Z. Fan, *Nano Energy*, 2015, **12**, 141–151.
29 K. Xiao, L. X. Ding, H. Chen, S. Wang, X. Lu and H. Wang, *J. Mater. Chem. A*, 2016, **4**, 372–378.
30 Y. Liu, Y. Z. Wang, G. X. Zhang, W. Liu, D. H. Wang and Y. G. Dong, *Mater. Lett.*, 2016, **176**, 60–63.
31 K. Wang, R. Yan, N. Zhao, X. D. Tian, X. Li, S. W. Lei, Y. Song, Q. G. Guo and L. Liu, *Mater. Lett.*, 2016, **174**, 249–252.
32 L. Wei, K. Tian, Y. Y. Jin, X. Y. Zhang and X. Guo, *Microporous Mesoporous Mater.*, 2016, **227**, 210–218.
33 S. J. Archibald, S. L. Atkin, W. Bras, A. Diego-Taboada, G. Mackenzie, J. F. W. Mosselmans, S. Nikitenko, P. D. Quinn, M. F. Thomas and N. A. Young, *J. Mater. Chem. B*, 2014, **2**, 945–959.
34 A. Diego-Taboada, L. Maillet, J. H. Banoub, M. Lorch, A. S. Rigby, A. N. Boa, S. L. Atkin and G. Mackenzie, *J. Mater. Chem. B*, 2013, **1**, 707–713.
35 A. Diego-Taboada, P. Cousson, E. Raynaud, Y. K. Huang, M. Lorch, B. P. Binks, Y. Queneau, A. N. Boa, S. L. Atkin, S. T. Beckett and G. Mackenzie, *J. Mater. Chem.*, 2012, **22**, 9767–9773.
36 R. C. Mundargi, M. G. Potroz, J. H. Park, J. Seo, E. L. Tan, J. H. Lee and N. J. Cho, *Sci. Rep.*, 2016, **6**, 19960–19973.
37 Y. Korenblit, M. Rose, E. Kockrick, L. Borchardt, A. Kvit, S. Kaskel and G. Yushin, *ACS Nano*, 2010, **4**, 1337–1344.
38 G. N. Yushin, E. N. Hoffman, A. Nikitin, H. H. Ye, M. W. Barsoum and Y. Gogotsi, *Carbon*, 2005, **43**, 2075–2082.
39 A. C. Ferrari and J. Robertson, *Phys. Rev. B: Condens. Matter Mater. Phys.*, 2000, **61**, 14095–14107.
40 K. Kumar, R. K. Saxena, R. Kothari, D. K. Suri, N. K. Kaushik and J. N. Bohra, *Carbon*, 1997, **35**, 1842–1844.
41 J. P. Paraknowitsch, J. Zhang, D. Su, A. Thomas and M. Antonietti, *Adv. Mater.*, 2010, **22**, 87–92.
42 K. Balakumar, R. Sathish and N. Kalaiselvi, *Electrochim. Acta*, 2016, **209**, 171–182.
43 V. Sahu, S. Grover, B. Tulachan, M. Sharma, G. Srivastava, M. Roy, M. Saxena, N. Sethy, K. Bhargava, D. Philip, H. Kim, G. Singh, S. K. Singh, M. Das and R. K. Sharm, *Electrochim. Acta*, 2015, **160**, 244–253.
44 Rajeshwarisivaraj, S. Sivakumar, P. Senthilkumar and V. Subburam, *Bioresour. Technol.*, 2001, **80**, 233–235.
45 J. Gamby, P. L. Taberna, P. Simon, J. F. Fauvarque and M. Chesneau, *J. Power Sources*, 2001, **101**, 109–116.
46 D. Yang, A. Velamakanni, G. Bozoklu, S. Park, M. Stoller, R. D. Piner, S. Stankovich, I. Jung, D. A. Field, C. A. Ventrice and R. S. Ruoff, *Carbon*, 2009, **47**, 145–152.

47 Z. Xu, X. Zhuang, C. Yang, J. Cao, Z. Yao, Y. Tang, J. Jiang, D. Wu and X. Feng, *Adv. Mater.*, 2016, **28**, 1981–1987.
48 T. Lin, I.-W. Chen, F. Liu, C. Yang, H. Bi, F. Xu and F. Huang, *Science*, 2015, **350**, 1508–1513.
49 J. W. Patrick, *Porosity in Carbons: Characterization and Applications*, Wiley, 1995.
50 J. Segalini, E. Iwama, P. L. Taberna, Y. Gogotsi and P. Simon, *Electrochem. Commun.*, 2012, **15**, 63–65.
51 N. Jackel, D. Weingarth, A. Schreiber, B. Kruner, M. Zeiger, A. Tolosa, M. Asian and V. Presser, *Electrochim. Acta*, 2016, **191**, 284–298.
52 J. Chmiola, G. Yushin, Y. Gogotsi, C. Portet, P. Simon and P. L. Taberna, *Science*, 2006, **313**, 1760–1763.
53 M. Seredych, M. Koscinski, M. Sliwinska-Bartkowiak and T. J. Bandosz, *ACS Sustainable Chem. Eng.*, 2013, **1**, 1024–1032.
54 J. H. Hou, C. B. Cao, F. Idrees and X. L. Ma, *ACS Nano*, 2015, **9**, 2556–2564.
55 P. Hao, Z. H. Zhao, Y. H. Leng, J. Tian, Y. H. Sang, R. I. Boughton, C. P. Wong, H. Liu and B. Yang, *Nano Energy*, 2015, **15**, 9–23.
56 W. Q. Tian, Q. M. Gao, Y. L. Tan, K. Yang, L. H. Zhu, C. X. Yang and H. Zhang, *J. Mater. Chem. A*, 2015, **3**, 5656–5664.
57 J. L. Chang, Z. Y. Gao, X. R. Wang, D. P. Wu, F. Xu, X. Wang, Y. M. Guo and K. Jiang, *Electrochim. Acta*, 2015, **157**, 290–298.
58 C. L. Long, D. P. Qi, T. Wei, J. Yan, L. L. Jiang and Z. J. Fan, *Adv. Funct. Mater.*, 2014, **24**, 3953–3961.
59 L. Li, Q. F. Zhong, N. D. Kim, G. D. Ruan, Y. Yang, C. T. Gao, H. L. Fei, Y. L. Li, Y. S. Ji and J. M. Tour, *Carbon*, 2016, **105**, 260–267.
60 K. Zhou, W. J. Zhou, Y. P. Du, X. J. Liu, Y. H. Sang, W. Li, J. Lu, H. Liu and S. W. Chen, *Sci. Adv. Mater.*, 2015, **7**, 571–578.
61 L. F. Chen, Z. H. Huang, H. W. Liang, H. L. Gao and S. H. Yu, *Adv. Funct. Mater.*, 2014, **24**, 5104–5111.
62 H. W. Liang, Z. Y. Wu, L. F. Chen, C. Li and S. H. Yu, *Nano Energy*, 2015, **11**, 366–376.
63 D. L. Yan, S. C. Li, G. S. Zhu, Z. M. Wang, H. R. Xu and A. B. Yu, *Mater. Lett.*, 2013, **95**, 164–167.
64 F. E. Atalay, D. Asma, E. Aydogmus, H. Turanci and H. Kaya, *Acta Phys. Pol., A*, 2014, **125**, 235–237.
65 L. Y. Gong, X. H. Liu, L. H. Su and L. Q. Wang, *J. Solid State Electrochem.*, 2012, **16**, 297–304.
66 L. F. Chen, Z. H. Huang, H. W. Liang, Q. F. Guan and S. H. Yu, *Adv. Mater.*, 2013, **25**, 4746–4752.
67 P. Hao, Z. Zhao, Y. Leng, J. Tian, Y. Sang, R. I. Boughton, C. Wong, H. Liu and B. Yang, *Nano Energy*, 2015, **15**, 9–23.
68 J. Chang, Z. Gao, X. Wang, D. Wu, F. Xu, X. Wang, Y. Guo and K. Jiang, *Electrochim. Acta*, 2015, **157**, 290–298.
69 W. Liu, X. Li, M. Zhu and X. He, *J. Power Sources*, 2015, **282**, 179–186.
70 D.-W. Park, N. A. Cañas, M. Schwan, B. Milow, L. Ratke and K. A. Friedrich, *Curr. Appl. Phys.*, 2016, **16**, 658–664.
71 Z. Yu, M. McInnis, J. Calderon, S. Seal, L. Zhai and J. Thomas, *NanoEnergy*, 2015, **11**, 611–620.
72 Y. Jiang, J. Yan, X. Wu, D. Shan, Q. Zhou, L. Jiang, D. Yang and Z. Fan, *J. Power Sources*, 2016, **307**, 190–198.
73 C. H. Kim and B.-H. Kim, *J. Power Sources*, 2015, **274**, 512–520.
74 Z. Y. Li, M. S. Akhtar and O.-B. Yang, *J. Alloys Compd.*, 2015, **653**, 212–218.
75 J. Patiño, N. López-Salas, M. C. Gutiérrez, D. Carriazo, M. L. Ferrer and F. del Monte, *J. Mater. Chem. A*, 2016, **4**, 1251–1263.
76 R. R. Salunkhe, J. Lin, V. Malgras, S. X. Dou, J. H. Kim and Y. Yamauchi, *Nano Energy*, 2015, **11**, 211–218.
77 D. P. Dubal, N. R. Chodankar, Z. Caban-Huertas, F. Wolfart, M. Vidotti, R. Holze, C. D. Lokhande and P. Gomez-Romero, *J. Power Sources*, 2016, **308**, 158–165.
78 Y. Sun, Y. Cheng, K. He, A. Zhou and H. Duan, *RSC Adv.*, 2015, **5**, 10178–10186.
79 P. H. Jampani, O. Velikokhatnyi, K. Kadakia, D. H. Hong, S. S. Damle, J. A. Poston, A. Manivannan and P. N. Kumta, *J. Mater. Chem. A*, 2015, **3**, 8413–8432.
80 M. Liu, W. W. Tjiu, J. Pan, C. Zhang, W. Gao and T. Liu, *Nanoscale*, 2014, **6**, 4233–4242.
81 Y. Wang, Z. Shi, Y. Huang, Y. Ma, C. Wang, M. Chen and Y. Chen, *J. Phys. Chem. C*, 2009, **113**, 13103–13107.
82 L. T. Le, M. H. Ervin, H. Qiu, B. E. Fuchs and W. Y. Lee, *Electrochem. Commun.*, 2011, **13**, 355–358.
83 D. Sun, X. Yan, J. Lang and Q. Xue, *J. Power Sources*, 2013, **222**, 52–58.
84 X. Sun, P. Cheng, H. Wang, H. Xu, L. Dang, Z. Liu and Z. Lei, *Carbon*, 2015, **92**, 1–10.